Article

Investigating the Metallic Nanoparticles Decoration on Reduced Graphene Oxide-Based Sensors Used to Detect Sulfur Dioxide

Elisa Ruiz [1], Christelle Varenne [1], Bruno S. De Lima [2], Thiaka Gueye [1], Alain Pauly [1], Jérôme Brunet [1], Valmor R. Mastelaro [2] and Amadou L. Ndiaye [1,*]

1 Université Clermont Auvergne, Clermont Auvergne INP, CNRS, Institut Pascal, F-63000 Clermont-Ferrand, France; elisa.ruiz206@gmail.com (E.R.); christelle.varenne@uca.fr (C.V.); thiakagueyenne@gmail.com (T.G.); alain.pauly@uca.fr (A.P.); jerome.brunet@uca.fr (J.B.)

2 Sao Carlos Institute of Physics, University of Sao Paulo, São Carlos 565-905, SP, Brazil; delimabs@unicamp.br (B.S.D.L.); valmor@ifsc.usp.br (V.R.M.)

* Correspondence: amadou.ndiaye@uca.fr

Abstract: This paper presents the impact of the decoration of reduced graphene oxide (rGO) with metallic nanoparticles to detect sulfur dioxide (SO_2). Copper and platinum were employed to produce metal nanoparticles (NPs) for the chemical and physical decoration of rGO to form the nanocomposites (rGO/NPs). We optimized NP loading by varying the concentrations of metal ions and deposition times for chemical and physical decoration, respectively. The chemical decoration presents a random nanoparticle distribution on the rGO surface with a broad particle size distribution (1 to 100 nm with a majority less than 40 nm). In comparison, the physical decoration presents uniformly distributed nanoparticles with particles of a size between 1 and 20 nm, with a majority less than 10 nm. The chemically decorated structures present the best gas responses and show that lower NP loading provides better responses. The nanocomposites present responses owing to a better synergy between NPs and the rGO surface, combined with the catalytic action of the NPs on the rGO. The physical decoration allows higher NP surface coverage than the chemical one but implies a lower remaining rGO naked surface for gaseous molecule interaction. These results illustrate that the NPs' surface and the uncovered rGO contribute to the gas response.

Keywords: rGO; nanoparticles; nanocomposites; functionalization; gas sensors; SO_2; NPs loading; physical decoration; chemical decoration

1. Introduction

In the field of nanomaterials, the unique properties of 2D materials have recently placed them in a tremendous position. Among these 2D materials, graphene, a one-atom-thick layer 2D material, has been regarded as one of the most promising candidates as it shows remarkable properties [1–5]. Graphene is an innovative material with versatile uses due to its two-dimensional planar structure, large specific surface area, and electronic properties [6]. Despite the existence of multiple methods to produce high-quality graphene films in a controlled way, mass production remains an issue [7]. Additionally, the use of graphene for practical applications, such as resistive gas sensors, has encountered difficulties due to its zero band gap [2,8]. As alternatives to pure graphene, graphene derivatives such as graphene oxide (GO) and reduced graphene oxide (rGO) are viable solutions. Alternative methodologies produce GO and rGO nanomaterials. Compared to graphene and rGO, GO presents an economic advantage due to cost effectiveness through mass production [9] and much easier processability via solution phase preparation and functionalization due to the surface oxygenated groups [1,4,10]. In the field of sensors, both GO and rGO have shown a promising future [11,12]. If GO gives the benefit of being dispersible in water, rGO meets sensor material properties for chemo-resistors since its conductivity is significantly increased compared to that of GO.

Nevertheless, generated oxygen-containing functional groups simultaneously activate the sites for sensing purposes, increase the gap, and develop defects [2,3]. Chemical and physical decorations can also increase the rGO gas sensitivity. Nowadays, GO and rGO materials are widely used to develop novel nanocomposites made of GO or rGO matrix combined with nanoparticles to target gaseous pollutants [13–16]. Associating rGO and nanoparticles (NPs) by physical or chemical methods gives rise to nanocomposites (rGO/NPs).

Pollutant gases are a worldwide general problem in terms of environmental and climate change concerns. Among the pollutants, sulfur-containing compounds are critical since they seriously impact health and the environment [17–19]. The case of SO_2 is problematic since it is generated by many industrial processes (fossil-based energy production, bleaching agents in industrial processes), natural processes (heating, volcanoes, wildfire, paper, wood), and homemade processes [20]. Therefore, developing sensors for detecting SO_2 is still relevant in this field. Regarding material development, the use of graphene derivatives as sensor material to detect SO_2 is still in demand. Among the graphene derivatives, the elaboration of nanocomposites prepared from graphene and nanoparticles has been developed worldwide due to the huge development of nanocomposite preparation by decoration and functionalization. Chemical decoration/functionalization is achieved using an in-situ method, where metal ion nanoparticles are directly reduced into the rGO surface using a chemical method such as metallic ion reduction. However, they can also be obtained using an ex-situ method by preparing separately synthesized nanoparticles and rGO material and mixing them to form nanocomposites. In the physical method, however, nanoparticles are directly deposited on the rGO or GO surface, and this method can be achieved simply by using a thermal evaporation technique. The nanocomposite materials offer superior sensing properties than their individual components and are ideal for developing sensors or new sensing materials. These composites display synergistic properties mainly arising from building a matching interface between the different constituents (NPs and rGO).

Furthermore, using such nanoparticles could be beneficial for lowering the aggregation of graphene nanosheets through intercalation [21]. Importantly, the NPs formed at the surface of the rGO act as spacers and increase the distance separating graphene sheets. In this way, the NPs maintain a high specific surface area [22] and provide, at the same time, accessible graphene surfaces for gaseous molecules. Therefore, regarding the field of sensors, such nanoparticles can act as catalysts for enhancing the reactivity with pollutants [23]. Finally, the decoration of the rGO by nanoparticles can significantly improve the electrical conductivity. For instance, using rGO/AuNPs as an electrochemical sensor has been shown to improve energy transfer compared to rGO or AuNPs individually [24]. Gutes et al. used a simple deposition method to prepare graphene/NPs (with different metal nanoparticles), among which the graphene/AuNPs showed promising sensing behavior towards H_2S [25]. Scroccarello et al. observed that under identical experimental conditions, other metals used for the nanoparticle functionalization would yield different morphologies, sizes, and distributions [26], and result in composite materials with different behaviors. This result means that adjusting the morphologies and sizes of NPs can be used efficiently to correlate with the reactivity.

Additionally, the size distribution and density of NPs in hierarchical nanostructures where different nanoparticles were incorporated, present a catalytic effect since they improve electrical conductivity [27] and sensitivity for gas sensors [25,26]. The decoration of GO with nanoparticles also leads to different catalytic effects according to the metal used [28]. The graphene decoration by platinum NPs revealed its suitability for SO_2 detection [29,30]. In the same way, other NP (Au, Ag, etc.) decorations on different matrices offer a higher sensitivity to SO_2 detection, showing that NP decorations are the key [31,32]. Similarly, associating copper nanoparticles with graphene or other materials has also been described as a good strategy for developing SO_2 sensors [33,34]. Therefore, we will probe

the metal decoration based on two metallic nanoparticles (Pt and Cu) to target SO_2 detection by focusing on the preparation method, i.e., physical vs. chemical decoration.

In this study, we prepared rGO by chemical reduction of GO and used it as a matrix for decoration. We decorated the rGO by chemical reduction and physical decoration using thermal evaporation of metals. For the preparation of nanocomposites (rGO/NPs), we used different concentrations of metal ions to optimize the NP loading for the chemical decoration, and parallel to this, we used different deposition times to generate different NP loading for the physical decoration. The obtained nanocomposites were then tested for the detection of SO_2. We focused this study on chemically reduced rGO decorated physically and chemically with metal nanoparticles. So, after structural and morphological characterization, the material was drop-casted on inter-digitated electrodes to investigate the sensing response upon SO_2 exposure. After carefully analyzing the gas response, we evaluated the sensor performance with the best nanocomposite.

2. Materials and Methods

2.1. Materials, Solvents and Preparation

Ethanol (purity grade > 99%) was obtained from Aldrich and used without further purification. As-produced GO (modified Hummer's method) was purchased from ACS Materials and was used as received (purity grade ~ 99%) Sodium citrate tribasic dihydrate (purity grade > 99.0%) was obtained from Aldrich and used as received. For the chemical decoration, copper sulphate hydrate ($CuSO_4 \cdot H_2O$) and potassium tetrachloroplatinate (K_2PtCl_4) were obtained from Sigma Aldrich. Copper and platinum metals (powder, purity grade of 99%) used for the physical decoration by thermal evaporation were obtained from NEYCO. An FB15047, 60 W (Fisher Scientific France, Fisherbrand, Illkirch, France) was used for ultrasonic treatment.

2.2. Preparation of rGO

In our study, graphene oxide was reduced to rGO using sodium citrate as a reducing agent. In a typical procedure, 100 mg of GO was first dispersed in a mixture of 90 mL water and 20 mL ethanol and homogenized by alternating heating and ultrasonic treatment. The obtained dispersion was then heated at 100 °C before adding a citrate solution (1.0 g in 10 mL of water). This reaction mixture was thus maintained for 90 min while heating and then left under stirring overnight at room temperature. The obtained dispersion was then filtered under vacuum, washed with distilled water, and dried in ambient air.

2.3. Preparation of rGO/NPs by Chemical Decoration

The chemical decoration of reduced graphene oxide was carried out chemically using sodium borohydride ($NaBH_4$) as a reducing agent. The reducing agent for chemical decoration can also be a stabilizing/capping agent for metal ions during chemical decoration [35]. In a typical procedure, 5 mg of rGO were first dispersed in a water/ethanol mixture in a (1 vol/1 vol) volume proportion, i.e., 5 mL of each. The dispersion was then homogenized for 5 min by ultrasonic treatment before reduction reactions. The solutions of metallic ions ($CuSO_4$ in water or K_2PtCl_4 in water, both at x mg/mL; with x = 1, 2, 3, 4, 8) were then added to the dispersion and stirred at room temperature for 5–10 min. Here, different solutions of the metal ions (Cu^{2+} and Pt^{2+}) at different concentrations (1 mg/mL, 2 mg/mL, 3 mg/mL, 4 mg/mL, and 8 mg/mL) based on a volume solution of 5 mL each, were evaluated. The mixture was thus maintained at room temperature for 5 min and left under stirring at room temperature. The dispersion was then filtered under vacuum, washed with distilled water, and dried in ambient air. For clarity, in the following, the chemically decorated nanocomposites are termed rGO/$M_{xmg/mL}$ (with M, the metal, and x mg/mL representing the concentration).

2.4. Preparation of rGO/NPs by Physical Decoration

The physical decoration was obtained by thermal evaporation using a thermal evaporator (EDWARDS Auto 306, Edwards High Vaccuum International, Crawley, UK) equipped with a thin film deposition monitor (TM-350, MAXTEK INC, Cypress, CA, USA) to control the thickness. The deposition rate was set around 0.6–0.7 Å/s for Cu nanoparticle deposition and 0.3–0.5 Å/s for Pt nanoparticle deposition under high vacuum (2.3×10^{-6} mbar). The Cu and Pt nanoparticles were sputtered onto the rGO surface, forming nanoparticles. The evaporation time was used here to control the NP size or film thickness. The deposition parameter was adjusted by measuring the thicknesses given by the thickness monitor control (12 Å and 22 Å for Cu decoration and 25 Å and 50 Å for Pt decoration) upon varying the sputtering times. Thus, the sputtering time was set to 17 s (Cu 12 Å) and 37 s (Cu 22 Å) for Cu decoration and 83 s (Pt 25 Å) and 100 s (Pt 50 Å) for Pt decoration. So, in the following, the physically decorated samples will be referred to as $rGO/Cu_{12Å}$, $rGO/Cu_{22Å}$, $rGO/Pt_{25Å}$, and $rGO/Pt_{50Å}$. We decided to limit the deposition amount to these values to avoid the coalescence and NP merging that is observed at higher deposition amounts.

2.5. Material Characterizations

Scanning electron microscopy (SEM) and transmission electron microscopy (TEM) were carried out for structural characterization. SEM micrographs were acquired from a Carl Zeiss Supra (Zeiss microscopie, Oberkochen, Germany) scanning electron microscope with an acceleration voltage of 3 kV. The samples were prepared by depositing one drop of the dispersion on a copper foil and drying on a hotplate. TEM micrographs were obtained with a HITACHI H-7650 TEM (Hitachi, Berkshire, UK) operating at 80 kV. Similarly, the samples were prepared by depositing one drop of the dispersion on a carbon-based TEM grid and dried at room temperature. To realize the particle distribution as given in the SEM and TEM images, the software IMAGE J (version 1.53) was used. The counts represent the numbers of average particles with the same average size within a range.

Raman spectroscopy experiments were carried out in a Witec microscope equipped with a Nikon objective (Witec, Ulm, Germany), and the samples were excited by an ion Ar laser (wavelength of 514 nm). Raman signals of the samples were excited with an Nd:YAG laser (532 nm; 10 mW), and Raman light was detected by a high sensitivity, back-illuminated Peltier-cooled CCD behind a 600 groove/mm grating. The data were recorded in the wavenumber range from 600 to 3000 cm^{-1}. All measurements were carried out at room temperature.

For electrical characterization, interdigitated electrodes (IDEs) made of platinum screen printed on an alumina substrate, with an inter-electrode distance of 125 µm (width × length = 3 mm × 5 mm), were used. The electrical characterization was carried out by drop-casting a few drops of dispersion of rGO on interdigitated electrodes. The IDE support was placed on a hotplate to ensure rapid solvent evaporation. The current (I) versus voltage (V) measurement, i.e., I–V characteristic of the sensing device, was performed in a two-point configuration in ambient air employing a Keithley 2636 System Source Meter (Tektronix, Berkshire, UK) controlled by LabVIEW software (version LabVIEW 2022). The I−V graphs were obtained in the −1 V to +1 V range with a step voltage of 0.01 V.

2.6. rGO Layers' Preparation and Test Bench

To realize resistive sensors, the composite rGO/NPs were dispersed in a mixture of water/ethanol (1 vol/1 vol) and layered by drop-casting on the resistive IDEs transducer maintained at 85 °C for solvent evaporation.

The sensor test bench consists of a dilution bench comprising a sensor chamber, a pollutant source (gas cylinders), mass flow controllers for controlling the dilution and concentration, and a computer-assisted program monitored through LabVIEW software for data acquisition (see Scheme S1 Supporting Information). Ambient air was pumped and dried using a desiccator column as presented in Scheme S1 to produce purified dry air. The

gas source from gas cylinders was diluted with the purified dry air (relative humidity of 3% and 5%) to generate the desired concentration range and sent to the sensor chamber. The sensor chamber comprised sensors that were wired for electrical measurement. We used a Keithley 2700 multimeter to record the resistance measurement. The sensor response is defined as $\Delta R/R_0$ given in percentage (%) using the following formula:

$$\Delta R/R_0 \ (\%) = (R_0 - R_{gas})/R_0 \times 100,$$

In this formula, R_{gas} is the resistance under gas exposure, and R_0 is the resistance under dried air.

The response time (τ_{resp}) is the time needed to reach 90% of the maximum response amplitude, while recovery time (τ_{rec}) is the time required to recover 90% of the background signal. The sensitivity (S) of the sensors, which defines the sensor's response per unit concentration (ppm), is given by:

$$S = \Delta R/R_0 \ (\%)/\text{Concentration (ppm)}$$

If not otherwise indicated, all experiments were performed at room temperature. The experimental bench is displayed in Scheme S1 (see Supporting Information).

3. Results

3.1. Characterization of Chemically and Physically Decorated rGO/NPs

3.1.1. SEM and TEM Characterization

rGO is well adapted for decoration with nanoparticles since the remaining oxygen-containing functional groups are essential for incorporating ions or nanoparticle seeds via electrostatic interaction, for example. The SEM image of the rGO is presented in Figure 1A for comparison. Figure 1B,C shows the morphology of the chemically decorated rGO/NP composites obtained by SEM, while Figure 1D,E shows the morphology of the physically decorated rGO/NP composites obtained by TEM. Compared to Figure 1A, where a flat surface represents the rGO surface, distinct and grain-like structures are observed in Figure 1B,C as representing nanoparticles on the rGO. We can identify the Pt and Cu nanoparticles as small dots on the rGO structure at lower and higher magnifications. Bigger and aggregated NPs dominated the Cu-decorated rGO (Figure 1B), while the Pt-decorated rGO presents a smaller NP size (Figure 1C). The TEM analysis of the physically decorated rGO also reveals this structural organization, where the rGO nanosheets are covered with nanoparticles. Here again, bigger NPs dominated the Cu-decorated rGO (Figure 1D), while smaller NPs illustrated the physically Pt-decorated rGO (Figure 1E).

The differences between the physically and chemically decorated rGO arise mainly in the distribution of the nanoparticles on the surface. In fact, the rGO/NP composites obtained by physical decoration illustrated a structure where the NPs are evenly distributed around the exposed rGO surface. The diameter distributions of the nanoparticles are shown as insets in the SEM and TEM images. The size distribution also suggests that the nanoparticles are smaller but in a high-density configuration, as revealed in the figures of physical decoration.

The chemically decorated composites present morphologies where the NPs are inhomogeneously distributed on the surface of the rGO. Nevertheless, the nanoparticle size is bigger than the previous case, with many aggregates resulting from the chemical reduction, where nucleation is followed by further growth, which is the dominant mechanism. In fact, in the in-situ chemical reduction, primary nucleation is considered as seeds that are potential nucleation sites for further reduction, increasing the size of the nanoparticles in this way. Conversely, the metals evaporated from the source are evenly distributed on the surface in the physical decoration method. It is, for example, established that in the physical deposition process, the deposited Pt nucleates and grows into individual nanoparticles on the graphene surface during the metal deposition process through evaporation. This is due to a film growth mechanism in metal deposition where cohesive bonds between metal

atoms are stronger than adhesive bonds between the atoms and substrate [36]. However, larger nanoparticles can also form during physical decoration if enough thermal energy is brought to adsorbed metal nanoparticles. Pandey et al. explained this occurrence and suggested that treating the samples with sufficient thermal energy allows them to nucleate on lower energy sites randomly [37].
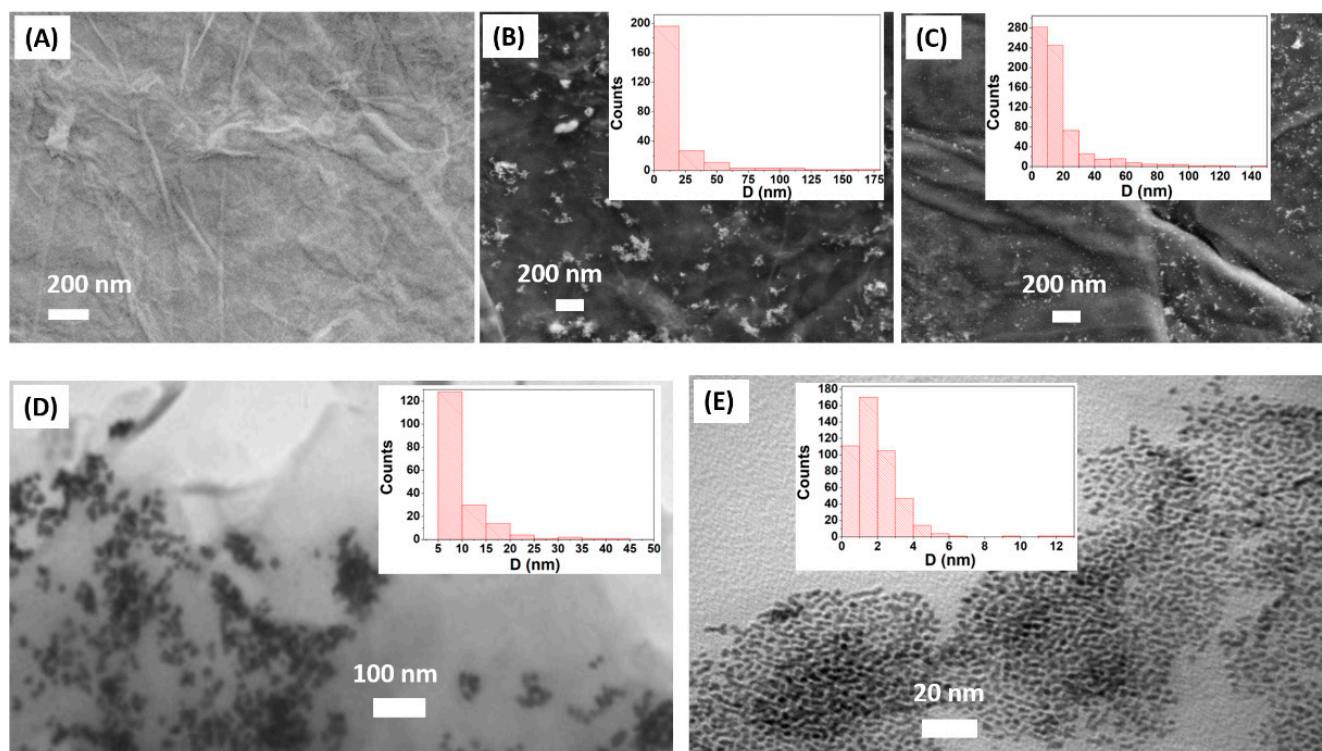

Figure 1. SEM images of rGO (**A**), and chemically decorated nanocomposites rGO/Cu (**B**) and rGO/Pt (**C**), and TEM images of physically decorated nanocomposites rGO/Cu$_{22Å}$ (**D**), and rGO/Pt$_{25Å}$ (**E**).

These morphological characterizations allow us to highlight the effectiveness of the decoration and present roughly the result of the two decoration methods and their resulting composite formation intended to develop sensor materials for sulfur dioxide detection. To sum up, the images of the physical decoration show that Pt and Cu nanoparticles are deposited uniformly on the rGO surface. At the same time, small aggregates of NPs and large aggregates of NPs dominate the SEM images of the Pt chemically decorated rGO and Cu chemically decorated rGO, respectively. Overall, the copper NPs are larger than the Pt NPs.

3.1.2. XRD and Raman Characterization

Figure 2 presents the XRD spectra of rGO and NP-decorated rGO. Characteristic peaks of the metals are well identified in the spectra, while a small shoulder represents the rGO's presence.

Comparison with JCPDS cards allows us to retrieve the data and state that Pt peaks are from the Pt NPs. The peaks located around 40.0°, 46.5°, 67.9°, and 81.7° are attributed to (111), (200), (220), and (311) plans, respectively [27,37].

For the rGO/Cu decoration, peaks are visible at 2θ equal to 29.8°, 36.7°, and 61.7°, which represent the (110), (111), and (220) of the Cu$_2$O [38], while other peaks at 2θ equal to 43.5° (111), 50.6 (200) and 74.2° (220) of the Cu [39], meaning that, in this case, both Cu and Cu2O are present. Such coexistence of Cu and Cu$_2$O after the chemical reduction of Cu ions has been previously reported even with the use of a stabilizing agent [40]. The results for the physical decoration are displayed in Figure S1. No specific peaks attributed

to the presence of the metallic nanoparticles could be detected in the XRD spectra. This result illustrates that the NPs were deposited but physical decoration does not present a well-defined crystalline structure.
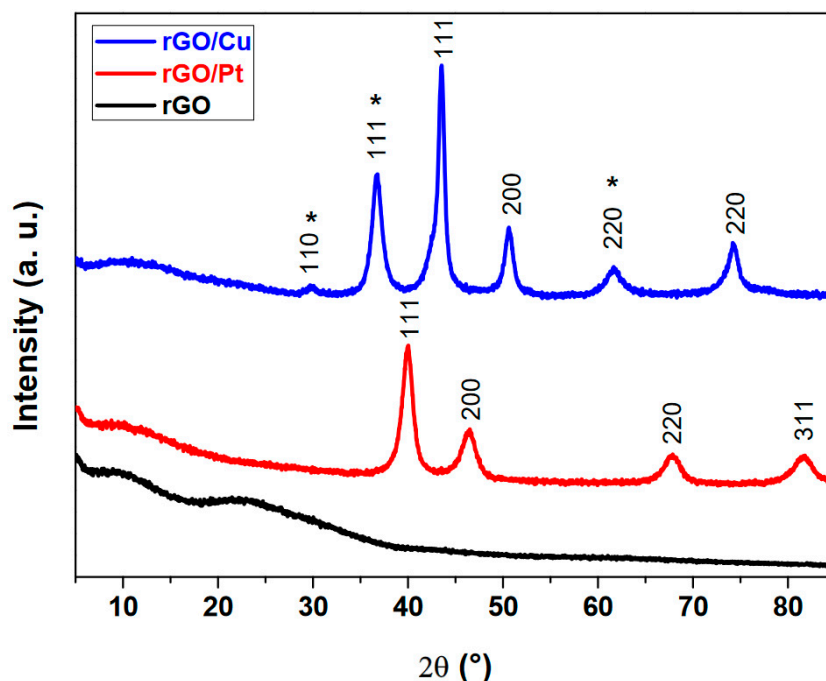

Figure 2. XRD spectra of the rGO and the chemically decorated nanocomposites rGO/Cu and rGO/Pt. Peaks labelled with * are for Cu_2O component in the rGO/Cu nanocomposites.

Raman is an exciting tool for understanding the transformation of carbon nanostructures since it enables the ability to quickly distinguish differences between carbon structures after a structural modification. Therefore, the changes in the decoration of the rGO by NPs were investigated by Raman spectroscopy, a sensitive technique regarding carbonaceous materials [41]. The measured spectra of the rGO samples and rGO/NP nanocomposites prepared chemically and physically are presented in Figure 3 and Figure S2, respectively. All spectra reveal the same G, D, and 2D bands in both materials. These three prominent characteristic peaks are generally observed in GO and rGO-based materials and represent specific features. The D band (disorder-induced band) localized around the 1350 cm^{-1} region is often related to the A1g breathing mode, which can have different origins, such as the extent of defects or disordered sp^3 carbon in the carbon sheet and impurities [42]. The G band (the tangential mode of graphitic structure) localized around the 1590 cm^{-1} region is related to the sp^2 carbon domains. It is often used to follow the restoration of the π-conjugated domains of sp^2 carbon atoms after the reduction of the GO into rGO. The 2D band can give information on the presence of single-layer or multi-layer graphene, depending on the shape and intensity of the 2D band ($\sim 2700 \text{ cm}^{-1}$) [43]. However, a decrease in the intensity of this band (2D) is also attributed to an increase in the density of defects or disorders [44]. The D peak of the rGO is slightly shifted from 1361 to 1358 cm^{-1} and 1357 cm^{-1} after decoration, and the G band also slightly shifts from 1584 cm^{-1} in the rGO to 1580 cm^{-1} and 1579 cm^{-1} after decoration. Such slight shifting in the bands is evidence of interaction between the different components [45]. Apart from the presence of these bands, the intensity ratio (ID/IG) is more reasonable in characterizing these structures correctly. In the rGO/NP structures, the ID/IG are estimated to be 1.47, 1.49, and 1.46 for the rGO, rGO/Cu, and rGO Pt, respectively, showing a slight difference. Here again, the Raman spectra of the rGO/NP samples in combination with the intensity ratio (ID/IG) indicate that decoration with NPs does not significantly affect the rGO.
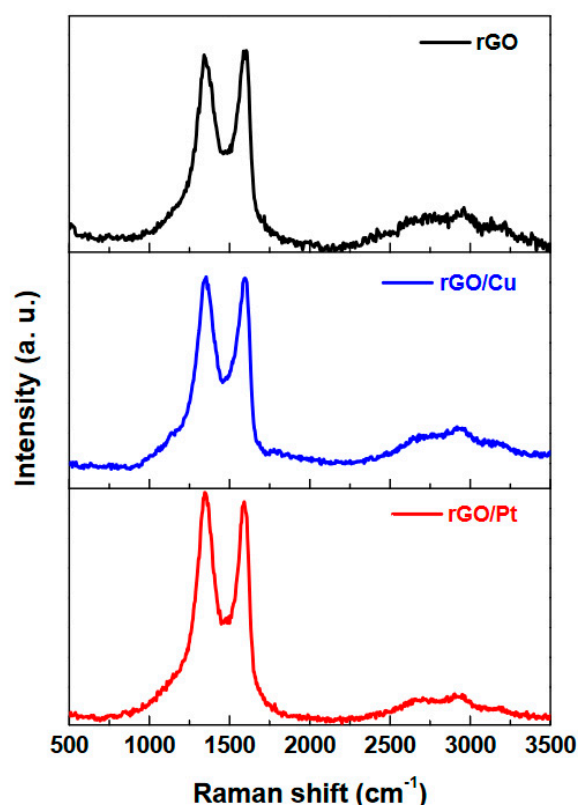
Figure 3. Raman spectra of the rGO, and the chemically decorated nanocomposites rGO/Cu and rGO/Pt.

As shown in Figure S2, the D peak of the rGO is shifted from 1357 to 1354 cm^{-1} and 1355 cm^{-1} after physical decoration, while the G band also slightly shifts from 1591 cm^{-1} in the rGO to 1586 cm^{-1} and 1587 cm^{-1} after physical decoration. The ID/IG are estimated to be 1.58, 1.35, and 1.38 for the rGO, rGO/Pt, and rGO/Cu, respectively, showing a significant difference compared to the chemical ones. From these results, it is observed that physical decoration affects the rGO structure more than chemical decoration. Such a result is attributed to the process of physical decoration that needs heating and vacuum treatment before deposition, affecting the structure. Additionally, physical decoration is not directed to a specific reaction site but proceeds randomly on the surface, depositing evenly at the surface.

3.1.3. Electrical Characterization

The electrical characterization of the rGO/NP composites is essential before realizing the sensors' structures. Figure 4 presents the electrical characterization obtained for rGO/NP composites decorated chemically. The current-voltage plots at room temperature for all nanocomposites present a linear current-voltage feature indicating an ohmic character of the chemically decorated rGO/NP composite. The current-voltage characterizations of the rGO/NP composite decorated physically also present an ohmic character (Figure S3).

After physical decoration, the sensors layer still has an ohmic behavior, showing that the conduction paths are conserved and active to guarantee the electron flow. The higher resistance value observed in the rGO/Cu$_{12Å}$ and rGO/Cu$_{22Å}$ indicates that no short-circuit resulting from NPs agglomeration and coalescence on the surface of the rGO materials has been observed. This result is due to a lower deposition rate and a lower amount of deposited material. In the case of platinum (Figure S4), the electrical characterization showed that at a higher decoration level, namely rGO/Pt$_{50Å}$, the resistance drops drastically to a value approaching the lower resistance material (approaching short-circuit). This effect is the

drawback of physical decoration since, without a net control of the deposition rate and the thickness, percolation can result in a lower resistance [46,47].
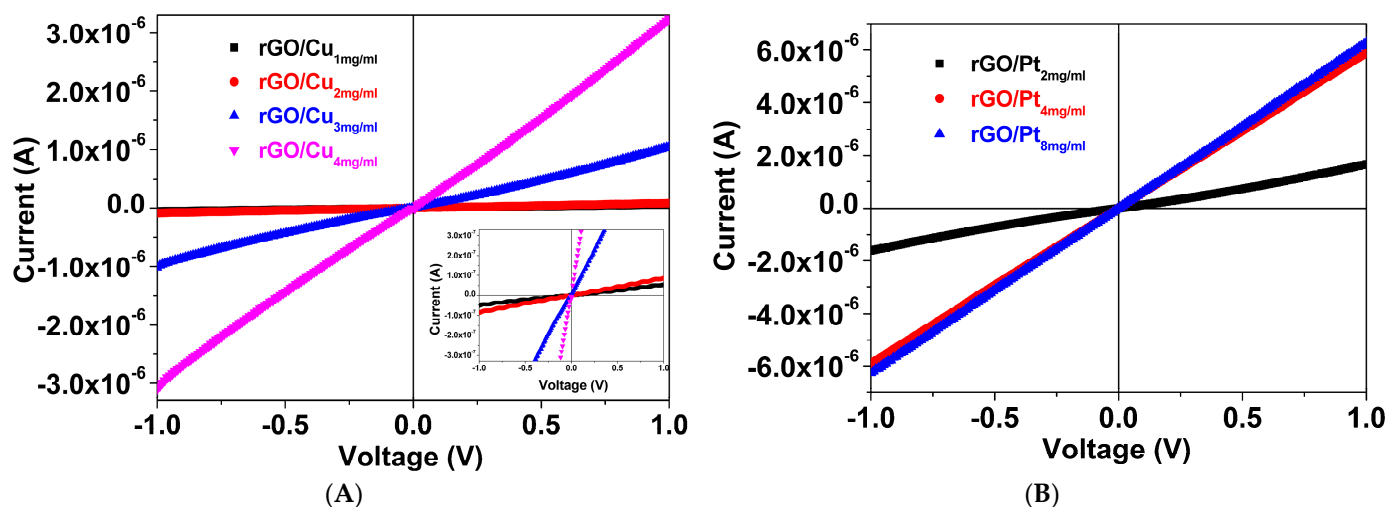

Figure 4. Current-voltage characteristics of rGO/Cu (**A**) and rGO/Pt (**B**) nanocomposites obtained by chemical decoration. The inset in Figure 4A shows a zoom on the y axis to highlight the overlapping curves (the red and black curves).

3.2. Sensors' Responses of the rGO/NP Nanocomposites Obtained by Chemical Decoration

3.2.1. Sensors' Responses of the Chemically Decorated rGO/Pt Nanocomposites

Figure 5 presents the sensor response of chemically decorated rGO/Pt nanocomposites exposed to SO_2. Figure 5A shows the sensor responses for the rGO/Pt$_{4mg/mL}$ and the rGO/Pt$_{8mg/mL}$ at room temperature. The response of the rGO/Pt at lower concentrations (<4 mg/mL) are not presented since they are not workable. The rGO/Pt$_{8mg/mL}$ presents a lower signal-to-noise ratio than rGO/Pt$_{4mg/mL}$.

The first exposure sequence in Figure 5A, shows a resistance decrease, illustrating an n-type material for rGO/Pt-based materials. The original rGO material itself presents a p-type material sign (not presented here). The prepared rGO is natively a p-type material, and the measured resistance at room temperature is attributed to hole majority carriers. It is also known that O_2 [48] (electron-withdrawing groups) and H_2O [49] favor p-type doping when adsorbed to graphene surface materials. The chemical and physical decoration sometimes create a type inversion from p-type to n-type. For example, it has been reported that AuNP decoration can invert graphene doping [50]. In this case, the AuNPs act as electron donors, leading to strong n doping of graphene. This type of inversion results from electron injection by metal nanoparticles into the rGO matrix.

NPs nucleate at the graphene surface preferentially on defects, impurities, and sites of oxygenated groups [51,52]. The NP decoration on the rGO surface contributes to tuning the work function and, therefore, facilitates the doping [53,54]. By doing so, they inject electrons into the rGO matrix and favor the n-type inversion. In addition, Xiang et al. showed that incorporating NPs can improve electrical conduction by charge transfer and tuning the Fermi level in graphene [55].

Figure 5B represents the sensor response of the chemically decorated rGO/Pt$_{8mg/mL}$ at room temperature and higher temperatures (50 °C, 80 °C, and 100 °C) at 80 ppm.

Increasing the operating temperature produced a lower response, as presented in Figure 5B. This result shows that temperature does not have a beneficial effect on the response of the sensors. After the experiments at higher temperatures, the sensors were re-exposed to the same gas at room temperature. The observed responses were even lower than the preliminary room temperature response and support the notion that the sensor responses are not improved with temperature treatment.
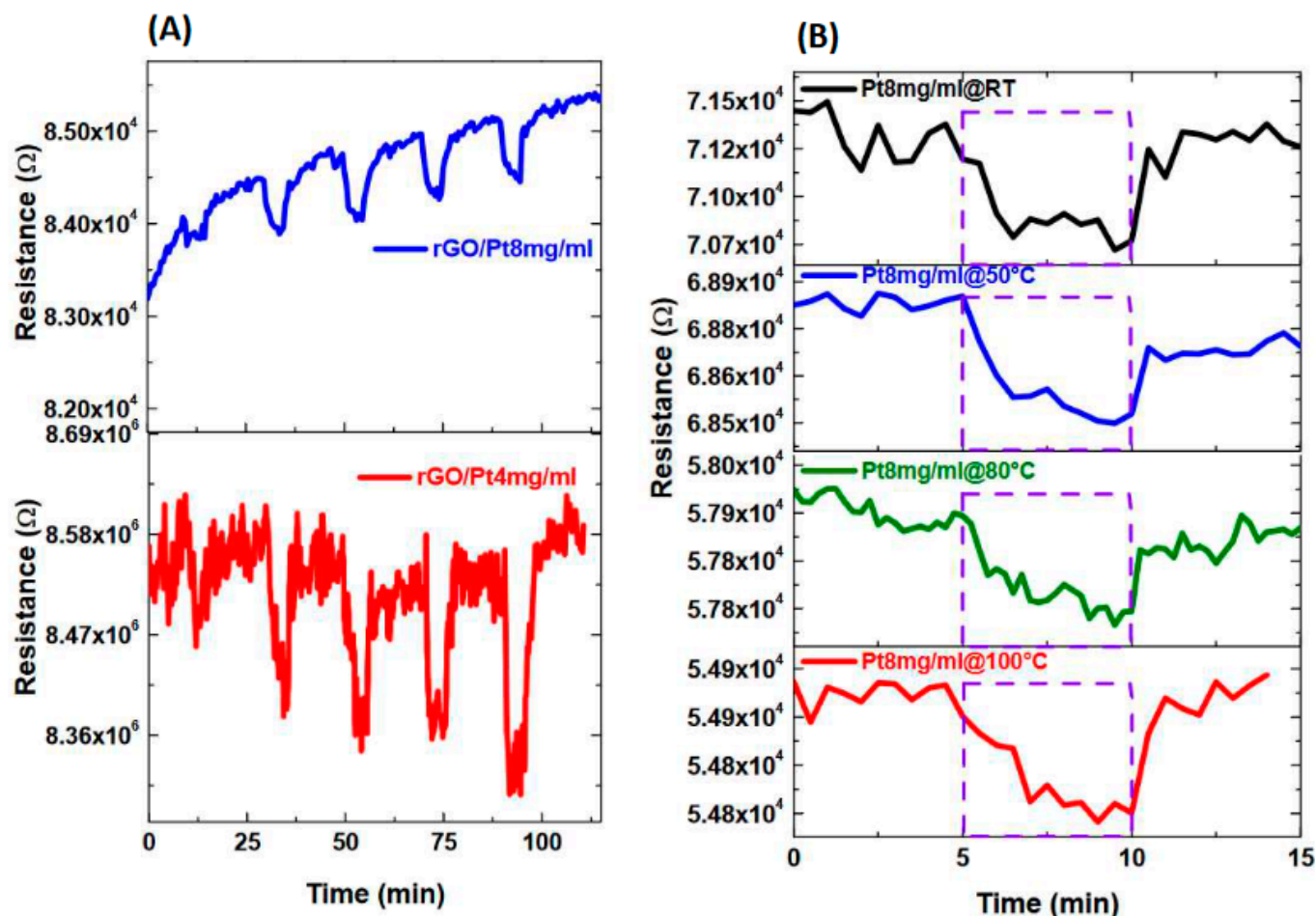
Figure 5. Sensor response of the chemically decorated rGO/Pt nanocomposites exposed to SO_2 concentrations in the range of 10–90 ppm at room temperature (**A**); and response to the 80 ppm exposure at different temperatures (**B**).

3.2.2. Sensors' Responses of the Chemically Decorated rGO/Cu Nanocomposites

Figure 6 presents the sensor response of chemically decorated rGO/Cu nanocomposites exposed to SO_2. Figure 6A shows the sensor responses for the chemically decorated rGO/Cu at different concentrations at room temperature. Compared to the case of rGO/Pt nanocomposites, all concentrations (1–4 mg/mL) yield measurable responses. The exposure shows a resistance decrease, illustrating an n-type material for rGO/Cu-based materials, as in the previous example. Figure 6B gives the corresponding calibration curves.

The precedent results showed that the rGO/Cu$_{2mg/mL}$ presents the best performances. Therefore, we used it for the following discussion. We then considered that the chemical decoration with 2 mg/mL (copper) is the optimal concentration for preparing the rGO/Cu-based materials. This result means that even if the incorporation of NPs improves the electrical conduction [55] and induces a catalytic effect, the amount of NPs is critical since a higher density of NPs on the graphene surface inhibits the sensor response. The sensor with a denser metal NP film exhibited lower gas responses due to a significant conduction path through the NPs metallic film rather than the graphene conduction channel [36]. This case is predominant when the physical decoration is processed and explains why physical decoration results in lower responses.

To improve the responses, we increased the operating temperature of the rGO/Cu$_{2mg/mL}$ sensor from RT to 110 °C, and the responses are presented in Figure 7. The calibration curves showed that the temperature did not improve the response, and an expected catalytic thermal activation did not occur. The room temperature response of the sensor

after the 110 °C experiment was lower than the preliminary room temperature, illustrating a detrimental effect of the temperature on the responses of the rGO/Cu$_{2mg/mL}$.
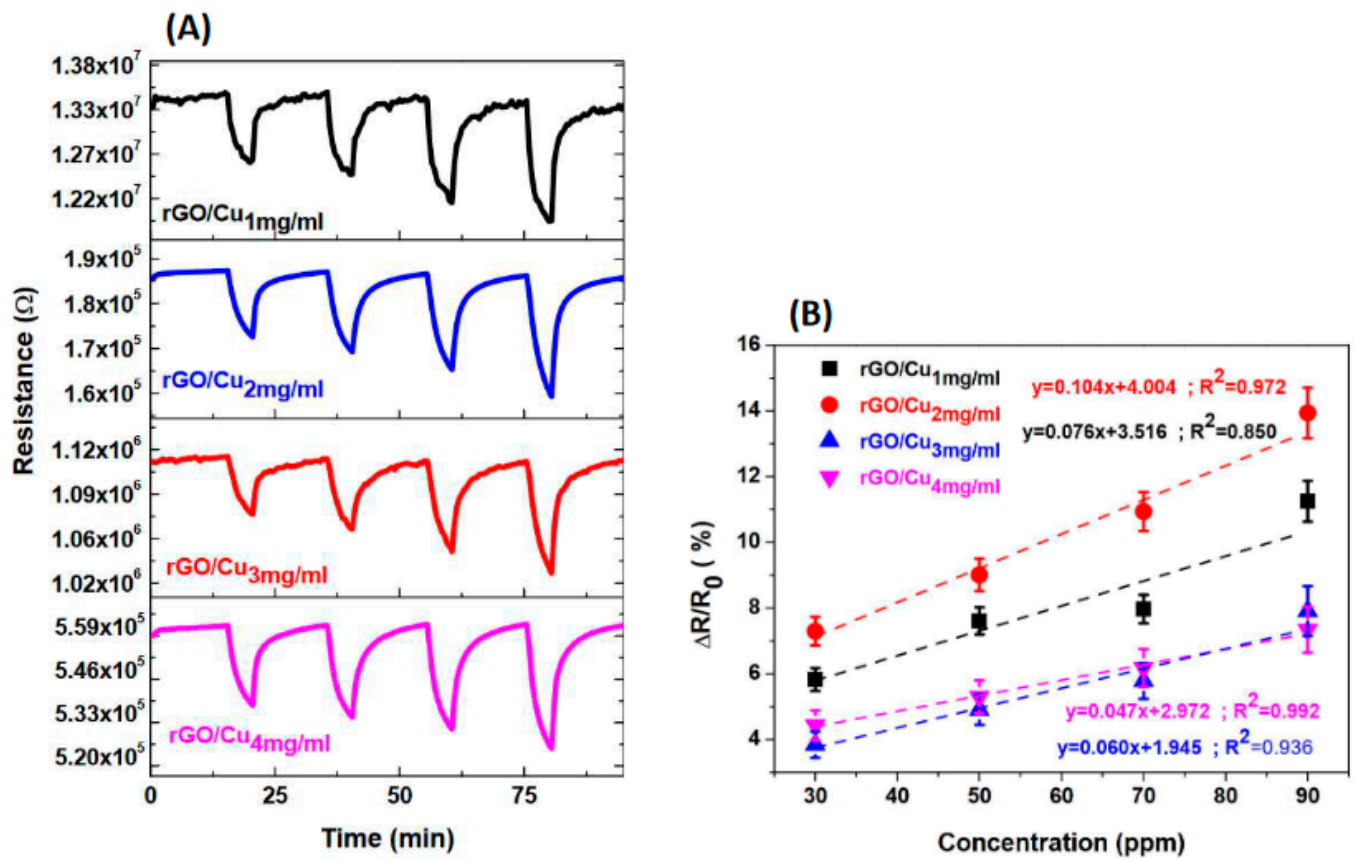

Figure 6. Sensor response of the chemically decorated rGO/Cu nanocomposites exposed to SO$_2$ concentrations in the 30–90 ppm range (**A**) and the corresponsding calibration curves (**B**).
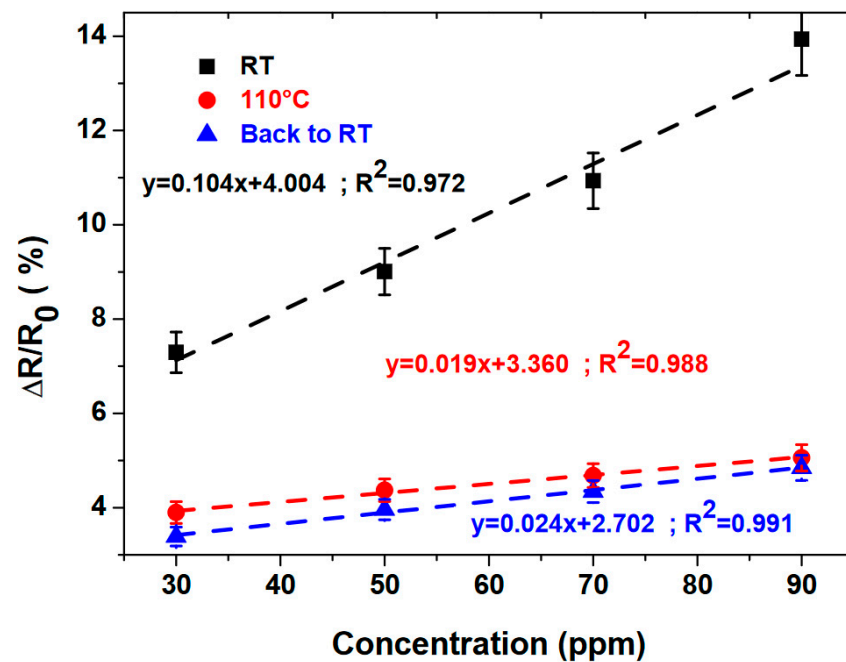

Figure 7. Response of the chemically decorated rGO/Cu$_{2mg/mL}$ exposed to SO$_2$ at room temperature, 110 °C and back again to room temperature.

3.3. Sensors' Responses of the rGO/NP Nanocomposites Obtained by Physical Decoration

We showed above that physical decoration presents better particle size distribution than chemical decoration. However, both decoration processes present ohmic characteristics regarding resistive behaviors. In the following paragraph, we will present the sensing properties of the physically decorated graphene-based material towards SO_2.

3.3.1. Sensors' Responses of the $rGO/Pt_{25Å}$ and $rGO/Pt_{50Å}$ Nanocomposites Obtained by a Physical Process

Figure S5 presents the sensor response of physically decorated rGO/Pt nanocomposites exposed to SO_2. The first exposure shows a resistance decrease, illustrating an n-type material for the $rGO/Pt_{25Å}$ and the $rGO/Pt_{50Å}$ based materials. Both sensors present a noisy signal at room temperature, making the response unexploitable. Therefore, using platinum decoration using a physical method can be seen as less sensitive for SO_2-based sensors. In front of the lack of exploitable response, the sensors are exposed to SO_2 at higher temperatures, but increasing the temperature did not improve the signal and responses at all.

3.3.2. Sensors' Responses of the $rGO/Cu_{12Å}$ and $rGO/Cu_{22Å}$ Nanocomposites Obtained by a Physical Process

For the rGO/Cu nanocomposites decorated physically, the responses are presented in Figure 8. In this case, the $rGO/Cu_{12Å}$ and the $rGO/Cu_{22Å}$ present responses that illustrate an n-type material with a resistance decrease under SO_2. Interestingly, the lower decorated sensor ($rGO/Cu_{12Å}$) presents a better response than the chemical decoration, where lower concentration ($rGO/Cu_{2mg/mL}$) presents a better response.
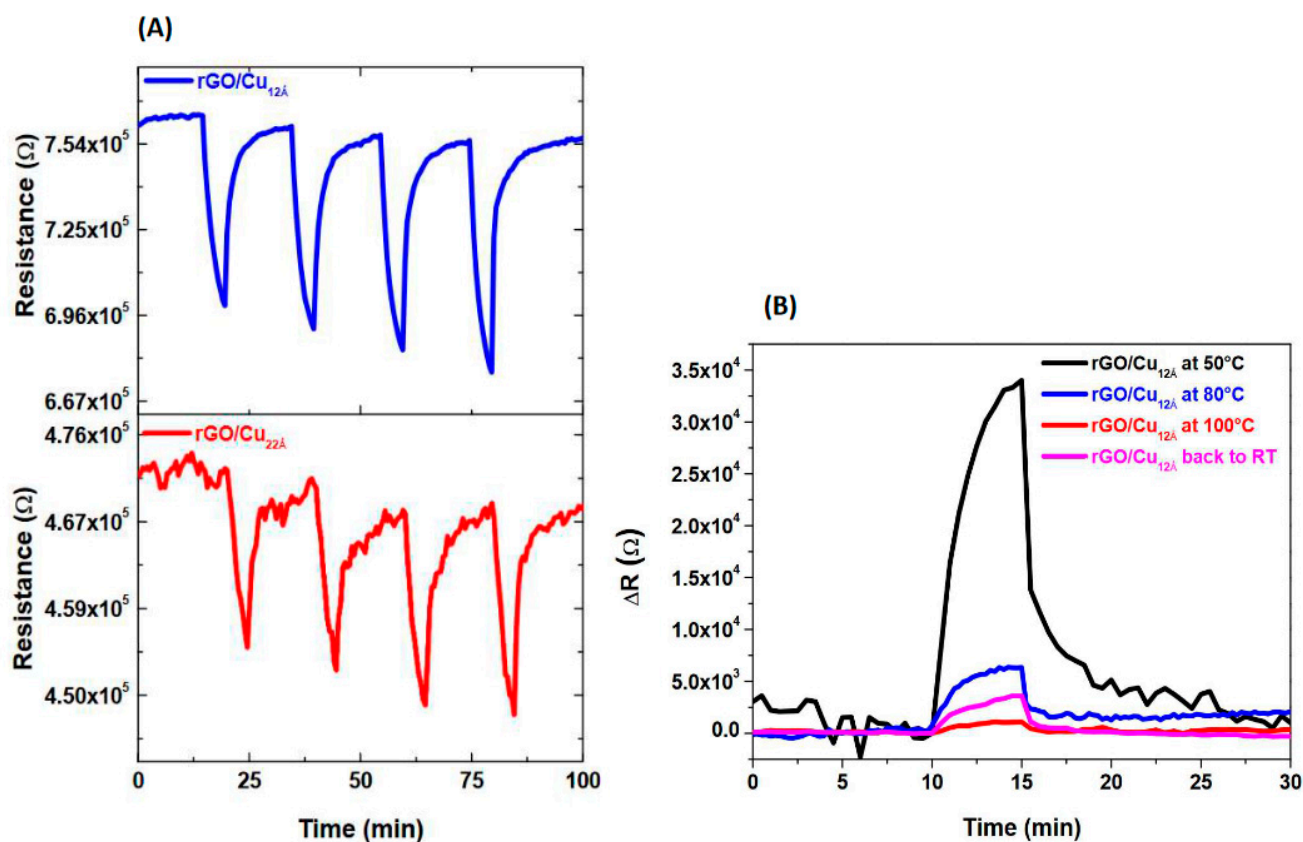

Figure 8. Response of the physically decorated $rGO/Cu_{12Å}$ and $rGO/Cu_{22Å}$ exposed to SO_2 at room temperature (**A**); and the response of the $rGO/Cu_{12Å}$ at room temperature and different temperatures (**B**).

Since the rGO/Cu$_{12\text{Å}}$ presents exciting features, we also increased the operating temperature during the exposure of the rGO/Cu$_{12\text{Å}}$ under SO$_2$ to improve the responses. Therefore, the sensors were exposed to 90 ppm of SO$_2$ at 50 °C, 80 °C, and 100 °C and back to RT. The results of these sequences are presented in Figure 8B. The response variations showed that apart from the exposure at 50 °C, the temperature does not improve the response, and an expected catalytic thermal activation does not occur. The re-exposure to room temperature after temperature experiments illustrates the degradation response with temperature. As in the case of the physical decoration of platinum, here again, the physical method provides less sensitive sensor materials for SO$_2$-based sensors using copper decoration.

At this point, two trends can be highlighted: (i) the chemical decoration gives better results than the physical one; (ii) the copper decoration presents a better response and represents the best nanocomposites. Regarding all of these results, combining the physical and chemical decoration and the obtained responses, the rGO/Cu$_{2\text{mg/mL}}$ was the best choice for detecting SO$_2$ gas. Therefore, the following steps will study the sensing performances with the rGO/Cu$_{2\text{mg/mL}}$ sensors obtained by the chemical method.

3.4. Sensors Performance of the Chemically Decorated rGO/Cu$_{2mg/mL}$

The rGO/Cu$_{2\text{mg/mL}}$ was tested for interfering gases, namely H$_2$S and CO, and the results are presented in the form of sensitivity. Figure 9 displays a histogram representing the sensitivity to different gases. The sensors present a sensitivity to SO$_2$ (0.104%/ppm) that is three times higher than the sensitivity towards H$_2$S, which was measured to be (0.03%/ppm), and a sensitivity eight times higher than the CO (0.017%/ppm). These results show that the rGO/Cu$_{2\text{mg/mL}}$ is suited for detecting SO$_2$ due to the lower cross-sensitivity to other gases. The NPs are active sites for gas adsorption; meanwhile, their catalytic properties enhance gas sensitivity since they promote interaction with some gases. The response time and the recovery time obtained from the room temperature experiment are estimated to be 230 s and 330 s, respectively, and the detection limit is evaluated to be 167 ppb.
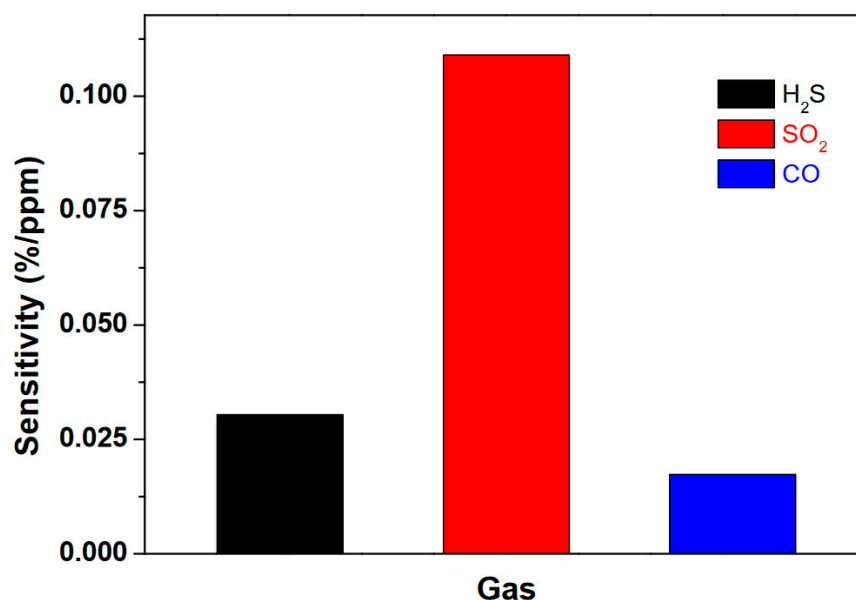

Figure 9. Cross-sensitivity histogram of the chemically decorated rGO/Cu$_{2\text{mg/mL}}$ sensor exposed to SO$_2$ and interfering gases H$_2$S and CO at room temperature.

From this graph, it can be stated that the rGO/Cu$_{2\text{mg/mL}}$ sensor presents a partial selectivity to SO$_2$.

This sensor was also evaluated in terms of long-term stability and humid conditions. The results are presented in Figures S6 and S7. For long-term stability, the rGO/Cu$_{2mg/mL}$ sensors were exposed to SO$_2$ using the same protocol in the range of 10–90 ppm and measurements were performed periodically, as displayed in Figure S6. The first exposure presented the lowest sensitivity and can be accounted for the preconditioning. After this phase, the sensors show reliable results since from the beginning and end of the experiment, the sensitivity only decreased about 13%, which can be considered acceptable. For the humidity experiment, the sensors showed that the higher humidity condition lead to a reduced response. At moderate humidity (3–10% RH), the resistance variation increased, while at higher humidity levels (>15%RH) the response decreased. In other words, the interaction with water dominates the adsorption of SO$_2$. So it means that there is a competition between humidity and SO$_2$ adsorption. It is important to point out that the surface of the nanocomposites still contain oxygenated groups (from rGO), and these can interact with water later. This result can be explained by the remaining oxygenated groups on the surface of the rGO, which interact with water from humid air, and this interaction dominates at higher humidity levels.

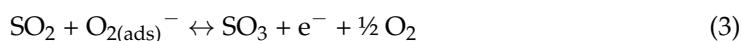## 4. Discussion

4.1. Mechanism of Interaction

We have seen in the above paragraph that the resistance decreases under SO$_2$ exposure. SO$_2$, as a reducing gas, will react with adsorbed oxygen atoms (Equations (1) and (2)). This reaction will produce SO$_3$ gas (Equation (3)) and re-inject the previously trapped electrons into the sensor layer (n-type), so the re-injected electrons contribute to an increase in the number of majority carriers that increases. Such an increase will induce a resistance decrease observed in the sensors' response profile in the response curves.

The role of adsorbed oxygen species should be considered when discussing the rGO-based materials used for sensing experiments [56]. When a rGO/NPs' sensing material is exposed to air as a carrier gas, the adsorption of molecular oxygen occurs preferentially on the defect sites, NPs, and remaining functional groups on the sensing surface. The oxygen adsorption and the following electrons trapping are associated with the following equations [57]:

$$O_2 \text{ (gas)} \leftrightarrow O_2 \text{ (ads)} \tag{1}$$

$$O_2 \text{ (ads)} + e^- \leftrightarrow O_2 \text{ (ads)}^- \tag{2}$$

Since we are dealing with room temperature experiments, among the general ionosorbed oxygen species encountered (O^{2-}, O$^-$, O$_2^-$), O$_2^-$ is the most probable existing species following Equation (2) [23,31,58,59]. In terms of conduction, both decorations generated better conduction than the rGO itself, and the resistance decreased in both cases. In terms of mechanism, molecular oxygen (O$_2$) adsorbs into the rGO/NPs structure and traps electrons by forming ionosorbed species (O$_2^-$). The SO$_2$, when adsorbed onto the surface, reacts with the created O$_2^-$ species by liberating electrons and gaseous SO$_3$ following the reaction below. Mechanistically, the NPs lower the work function of the rGO, facilitating the electrons' flow between the two materials. By doing so, they also contribute positively to facilitating the charge transfer. The NPs act as catalysts and receptors that attract gaseous species. Then, they initiate the interaction and accelerate the reactivity, meanwhile enhancing sensor sensitivity.

When the SO$_2$ enters the chamber, it interacts with the negatively charged oxygen ions adsorbed over the surface of the sensing film. As a result of this interaction, the formation of SO$_3$ occurs, and a negative charge (e$^-$) is then released into the sensing film, creating a conductivity increase of the sensing film i.e., resistance decrease.

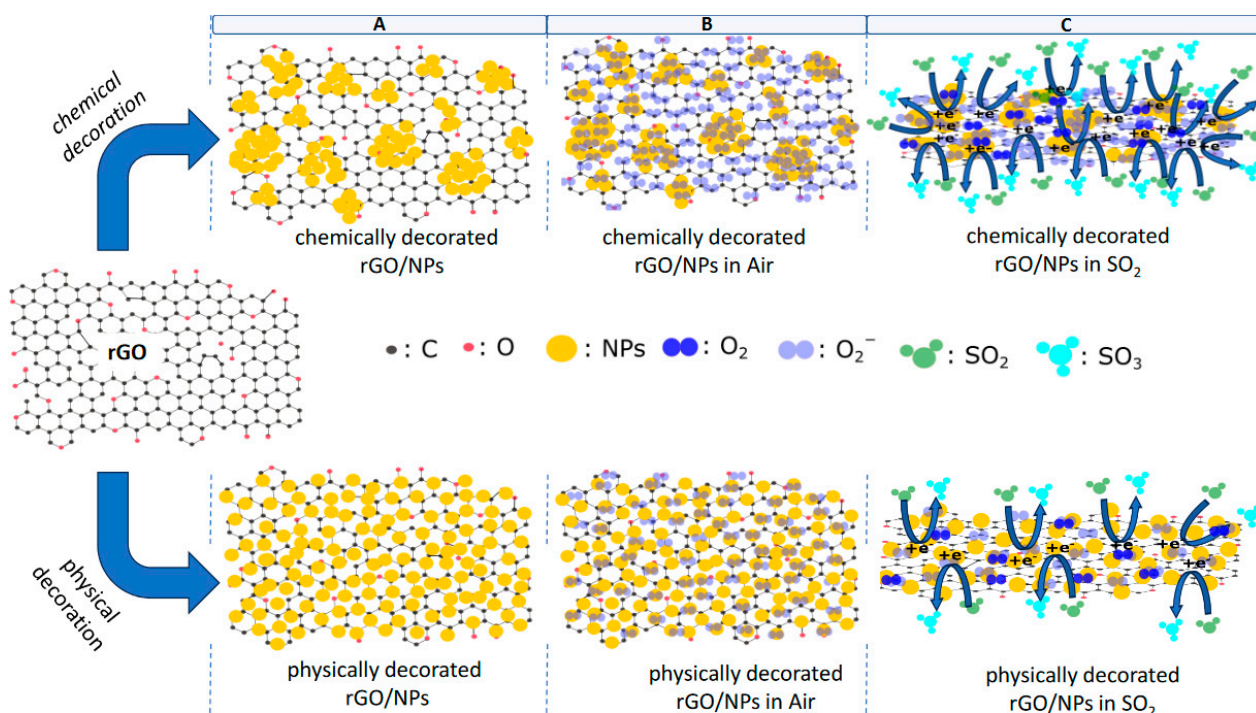$$SO_2 + O_{2(ads)}^- \leftrightarrow SO_3 + e^- + \tfrac{1}{2} O_2 \tag{3}$$

Furthermore, noble metal decoration enhances oxygen adsorption activation [46,60,61]. Therefore, the catalytic effect is enhanced by the presence of NPs on the rGO, and the

contribution of the NPs to the sensitivity enhancement is manifest. Such an effect is discussed and used to explain the sensitivity enhancement of decorated sensing material for SO_2 detection, even if the GO nanosheets presented good sensing performance for detecting SO_2 [62].

4.2. Chemical versus Physical Decoration

The use of graphene-based nanocomposites issuing from the metal nanoparticle decoration shows that metallic nanoparticles act as catalysts to increase the reaction between gases and graphene or rGO [11]. Additionally, nanoparticle decoration can enhance the conductivity of the rGO. The conductivity improvement facilitates the conducting path between rGO and metallic NPs. Even if the mechanism of reduction and growth is not well amended, authors agree, at least for chemical decoration, that the remaining oxygen functionalities of GO or rGO provide reactive nucleation sites [52]. These later evolved into seeds and finally grew once the metal ions were reduced into nanoparticles with the addition of a reducing agent [52]. Secondly, the NPs are formed essentially on structural defects in rGO and contribute to repairing the rGO skeleton by decorating the defects with NPs [63]. This effect is a kind of healing of the defective rGO and helps restore the conductivity.

Regarding the difference between the physical and chemical decoration in terms of response and sensitivity, we observed that the chemical decoration produces by far the best results. If we consider that the mechanism is identical, the different sensitivity can be attributed to differences in the structure since both decorations lead to ohmic behavior. To explain and understand the mechanism, Scheme 1 is used to summarize the two situations of decoration and their interactions with the gas. The upper panel represents the chemical decoration case while the lower panel represents that of the physical decoration. The different steps are labeled A, B, and C and represent the nanocomposites after fabrication (Step A), their reactivity in the air (Step B), and finally, their interaction with SO_2 gas (Step C).

Scheme 1. Schematic representation of the decoration and the interaction of the nanocomposites with SO_2 gas. The upper panel represents the chemical decoration and the lower panel represents the physical decoration in their different steps: Step A (fabrication), Step B (reactivity in air), and Step C (interaction with SO_2 gas).

Step A: In the chemical decoration route, the primary deposited nanoparticles behave like seeds and serve as future growing sites for incoming NPs. Therefore, the NPs easily form aggregates concentrated on specific areas (on the rGO) with this method, and as a consequence, many rGO areas remain uncovered (free of NPs). This case is represented in Scheme 1 (step A in the upper panel). The SEM and TEM confirmed this structural organization. The physical decoration, contrary to chemical decoration, is not oriented through specific surface sites. In the physical decoration, the NPs are formed on the surface and occupy almost all rGO surfaces (Scheme 1: step A in the lower panel). This is a result of the process of physical decoration, where the surface of the rGO is bombarded homogeneously by atoms evaporated by the metal source.

Step B: Regarding the NPs decoration, the physical method presents the best NP distribution and the smallest NP size (Scheme 1: step A in the lower panel), while the chemical decoration is more subject to aggregates and islands of NP formation (Scheme 1: step A in the upper panel). The consequence of their different surface coverage is that the remaining rGO surface is higher in the chemical than in the physical. Remember that NPs and the remaining rGO surface are additional active sites for gas adsorption. This means that in air, both surfaces are exposed to oxygen and produce ionosorbed oxygen species (Scheme 1: step B in the upper and lower panels). As the ionosorbed species are activating the reaction with SO_2, then the interaction occurs.

Step C: If the NPs are evenly distributed on the surface, as in the case of the physical decoration, then there are no additional active sites for gas adsorption to react with, and the sensor shows a lower sensitivity (Scheme 1: step C in the lower panel). The chemical decoration, a defect-oriented-reaction subject to aggregate formation, presents more available free rGO surface. This free rGO surface enhances the sensitivity since it offers more active sites for interaction.

Decorating the rGO surface by a chemical method is an optimal way to benefit from both the rGO surface and the NPs while engaging the catalytic effect of the NPs sitting on the rGO. In our case, the SO_2 molecules react with the $O_2{}^-$ adsorbed on the NPs surface [64] and $O_2{}^-$ adsorbed on the rGO surface [65] to form SO_3 (Scheme 1: step C in the upper and lower panels) and release the trapped electrons (Equation (3)).

It seems that the physical decoration cannot profit from such available free rGO surfaces even if the catalytic particles are everywhere on the surface. This situation can be analyzed as similar to the poisoning effect due to denser nanoparticle distribution, which finally hinders the rGO surface's reactivity. Remember also that decorating the rGO densely (higher decoration/coverage level) leads to a sensor that presents a much lower resistance and almost no significant response. With nanoparticle decoration, both the rGO surface and the NP distribution play an important role. These results follow previous reports highlighting the participation of the functional groups of the rGO in gas responses [65]. It is established that the rGO surface, because of its functional groups, can catalyze the adsorption of SO_2 and reduce the oxidation barrier leading to SO_3 formation [66]. With a higher decoration step and denser distribution, the synergetic effect gained from the two components (NPs and rGO) tends to disequilibrium and, therefore, does not favor an enhanced response. This result shows that decoration is essential for strengthening the responses, but the rGO (with the oxygen functional groups) is also necessary for sensing purposes.

5. Conclusions

In this study, we prepared rGO by chemical reduction of GO and then initiated metal nanoparticle decoration of the rGO matrix. We then explored two decoration methods to study the detection of SO_2 gas. The chemical decoration method is based on the direct reduction of nanoparticles onto the rGO surface employing chemical reduction. In contrast, the physical process of the metal nanoparticle decoration on the rGO's surface proceeds through evaporation. The morphological and physicochemical characterization highlights the effectiveness of the decoration. The images of the physical decoration show that

nanoparticles are deposited uniformly on the rGO surface while small aggregates of NPs and large aggregates of NPs dominate in the chemical decoration. The sensor's response showed that the chemical decoration presents the best responses compared to the physical ones. The copper NPs present better reactivity towards SO_2 than the Pt. The temperature does not seem to improve the chemical decoration, while a slightly higher temperature (50 °C) improves the response for the physical decoration. The results showed that the synergetic effect gained from the two components (NPs and rGO) is enhanced in the chemical method. At the same time, they are non-significant in the physical method due to lower rGO available surface. Decorating the rGO surface by a chemical method is an optimal way to benefit from both the free surface and NPs while engaging the catalytic effect of the NPs sitting on the rGO. The distribution of the NPs is important, but the free rGO surface is also essential for sensing. Therefore, an overly dense decoration of NPs 4wis detrimental to sensor response.

Institutional Review Board Statement: Not applicable.

Informed Consent Statement: Not applicable.

Data Availability Statement: Data are contained within the article and supplementary materials.

Conflicts of Interest: The authors declare no conflicts of interest.

References

1. Papageorgiou, D.G.; Kinloch, I.A.; Young, R.J. Mechanical properties of graphene and graphene-based nanocomposites. *Prog. Mater. Sci.* **2017**, *90*, 75–127. [CrossRef]
2. Avouris, P. Graphene: Electronic and Photonic Properties and Devices. *Nano Lett.* **2010**, *10*, 4285–4294. [CrossRef]
3. Duplock, E.J.; Scheffler, M.; Lindan, P.J.D. Hallmark of Perfect Graphene. *Phys. Rev. Lett.* **2004**, *92*, 225502. [CrossRef]

4. Smith, A.T.; LaChance, A.M.; Zeng, S.; Liu, B.; Sun, L. Synthesis, properties, and applications of graphene oxide/reduced graphene oxide and their nanocomposites. *Nano Mater. Sci.* **2019**, *1*, 31–47. [CrossRef]

5. Neto, A.H.C.; Guinea, F.; Peres, N.M.R.; Novoselov, K.S.; Geim, A.K. The electronic properties of graphene. *Rev. Mod. Phys.* **2009**, *81*, 109–162. [CrossRef]

6. Wu, J.; Lin, H.; Moss, D.J.; Loh, K.P.; Jia, B. Graphene oxide for photonics, electronics and optoelectronics. *Nat. Rev. Chem.* **2023**, *7*, 162–183. [CrossRef]

7. Ren, W.; Cheng, H.-M. The global growth of graphene. *Nat. Nanotechnol.* **2014**, *9*, 726–730. [CrossRef]

8. Donarelli, M.; Ottavi, L. ano, 2D Materials for Gas Sensing Applications: A Review on Graphene Oxide, MoS2, WS2 and Phosphorene. *Sensors* **2018**, *18*, 3638. [CrossRef]

9. Kong, W.; Kum, H.; Bae, S.-H.; Shim, J.; Kim, H.; Kong, L.; Meng, Y.; Wang, K.; Kim, C.; Kim, J. Path towards graphene commercialization from lab to market. *Nat. Nanotechnol.* **2019**, *14*, 927–938. [CrossRef]

10. Dai, J.; Wang, G.; Ma, L.; Wu, C. Study on the surface energies and dispersibility of graphene oxide and its derivatives. *J. Mater. Sci.* **2015**, *50*, 3895–3907. [CrossRef]

11. Tang, X.; Debliquy, M.; Lahem, D.; Yan, Y.; Raskin, J.-P. A Review on Functionalized Graphene Sensors for Detection of Ammonia. *Sensors* **2021**, *21*, 1443. [CrossRef]

12. Robinson, J.T.; Perkins, F.K.; Snow, E.S.; Wei, Z.; Sheehan, P.E. Reduced Graphene Oxide Molecular Sensors. *Nano Lett.* **2008**, *8*, 3137–3140. [CrossRef]

13. Abideen, Z.U.; Kim, J.-H.; Mirzaei, A.; Kim, H.W.; Kim, S.S. Sensing behavior to ppm-level gases and synergistic sensing mechanism in metal-functionalized rGO-loaded ZnO nanofibers. *Sens. Actuators B Chem.* **2018**, *255*, 1884–1896. [CrossRef]

14. Jin, L.; Chen, W.; Zhang, H.; Xiao, G.; Yu, C.; Zhou, Q. Characterization of Reduced Graphene Oxide (rGO)-Loaded SnO_2 Nanocomposite and Applications in C_2H_2 Gas Detection. *Appl. Sci.* **2017**, *7*, 19. [CrossRef]

15. Lun, D.; Xu, K. Recent Progress in Gas Sensor Based on Nanomaterials. *Micromachines* **2022**, *13*, 919. [CrossRef]

16. Tyagi, P.; Sharma, A.; Tomar, M.; Gupta, V. A comparative study of RGO-SnO_2 and MWCNT-SnO_2 nanocomposites based SO_2 gas sensors. *Sens. Actuators B Chem.* **2017**, *248*, 980–986. [CrossRef]

17. Wei, J.; Guo, X.; Marinova, D.; Fan, J. Industrial SO_2 pollution and agricultural losses in China: Evidence from heavy air polluters. *J. Clean. Prod.* **2014**, *64*, 404–413. [CrossRef]

18. Soeroso, N.N.; Intan, T.K.; Ichwan, M. Factors associated decrease of forced vital capacity on gas station employees exposed to sulfur dioxide (SO_2). *IOP Conf. Ser. Earth Environ. Sci.* **2019**, *245*, 012015. [CrossRef]

19. Chen, T.-M.; Kuschner, W.G.; Gokhale, J.; Shofer, S. Outdoor Air Pollution: Nitrogen Dioxide, Sulfur Dioxide, and Carbon Monoxide Health Effects. *Am. J. Med. Sci.* **2007**, *333*, 249–256. [CrossRef] [PubMed]

20. Braghiroli, F.L.; Bouafif, H.; Koubaa, A. Enhanced SO_2 adsorption and desorption on chemically and physically activated biochar made from wood residues. *Ind. Crops Prod.* **2019**, *138*, 111456. [CrossRef]

21. Xu, C.; Wang, X.; Zhu, J. Graphene–Metal Particle Nanocomposites. *J. Phys. Chem. C* **2008**, *112*, 19841–19845. [CrossRef]

22. Guo, Y.; Yang, X.; Ruan, K.; Kong, J.; Dong, M.; Zhang, J.; Gu, J.; Guo, Z. Reduced Graphene Oxide Heterostructured Silver Nanoparticles Significantly Enhanced Thermal Conductivities in Hot-Pressed Electrospun Polyimide Nanocomposites. *ACS Appl. Mater. Interfaces* **2019**, *11*, 25465–25473. [CrossRef] [PubMed]

23. Mirzaei, A.; Lee, J.-H.; Majhi, S.M.; Weber, M.; Bechelany, M.; Kim, H.W.; Kim, S.S. Resistive gas sensors based on metal-oxide nanowires. *J. Appl. Phys.* **2019**, *126*, 241102. [CrossRef]

24. Qi, M.; Zhang, Y.; Cao, C.; Zhang, M.; Liu, S.; Liu, G. Decoration of Reduced Graphene Oxide Nanosheets with Aryldiazonium Salts and Gold Nanoparticles toward a Label-Free Amperometric Immunosensor for Detecting Cytokine Tumor Necrosis Factor-α in Live Cells. *Anal. Chem.* **2016**, *88*, 9614–9621. [CrossRef] [PubMed]

25. Gutés, A.; Hsia, B.; Sussman, A.; Mickelson, W.; Zettl, A.; Carraro, C.; Maboudian, R. Graphene decoration with metal nanoparticles: Towards easy integration for sensing applications. *Nanoscale* **2012**, *4*, 438–440. [CrossRef] [PubMed]

26. Scroccarello, A.; Álvarez-Diduk, R.; Della Pelle, F.; de Carvalho Castro e Silva, C.; Idili, A.; Parolo, C.; Compagnone, D.; Merkoçi, A. One-Step Laser Nanostructuration of Reduced Graphene Oxide Films Embedding Metal Nanoparticles for Sensing Applications. *ACS Sens.* **2023**, *8*, 598–609. [CrossRef] [PubMed]

27. Darabdhara, G.; Amin, M.A.; Mersal, G.A.M.; Ahmed, E.M.; Das, M.R.; Zakaria, M.B.; Malgras, V.; Alshehri, S.; Yamauchi, Y.; Szunerits, S.; et al. Reduced graphene oxide nanosheets decorated with Au, Pd and Au–Pd bimetallic nanoparticles as highly efficient catalysts for electrochemical hydrogen generation. *J. Mater. Chem. A* **2015**, *3*, 20254–20266. [CrossRef]

28. Moafi, A.; Heidari, O.; Soltannia, B.; Wlodarski, W.; Shahi, F.; Parvin, P. Reduction of metal nanoparticle decorated flexible graphene oxide by laser at various temperatures and under selected atmospheres. *Carbon Trends* **2022**, *6*, 100140. [CrossRef]

29. Zhang, X.; Cui, H.; Gui, Y. Synthesis of Graphene-Based Sensors and Application on Detecting SF6 Decomposing Products: A Review. *Sensors* **2017**, *17*, 363. [CrossRef]

30. Rad, A.S.; Zareyee, D. Adsorption properties of SO_2 and O_3 molecules on Pt-decorated graphene: A theoretical study. *Vacuum* **2016**, *130*, 113–118.

31. Hsueh, T.-J.; Lee, S.-H. A La_2O_3 Nanoparticle SO_2 Gas Sensor that Uses a ZnO Thin Film and Au Adsorption. *J. Electrochem. Soc.* **2021**, *168*, 077507. [CrossRef]

32. Xu, H.; Li, J.; Fu, Y.; Li, P.; Luo, W.; Tian, Y. Ag/Ag_2S Nanoparticle-Induced Sensitization of Recovered Sulfur-Doped SnO_2 Nanoparticles for SO_2 Detection. *ACS Appl. Nano Mater.* **2020**, *3*, 8075–8087. [CrossRef]

33. Li, R.; Wang, S.; Li, S.; Zhao, F.; Dong, T.; He, P.; Yu, L.; Miao, J.; Fan, X. Cu-doped flower-like SnO$_2$ architecture toward promoting SO$_2$ detection: Fast equilibrium and low trace monitoring. *Sens. Actuators B Chem.* **2023**, *390*, 133953. [CrossRef]

34. Zhao, C.; Gong, H.; Niu, G.; Wang, F. Ultrasensitive SO$_2$ sensor for sub-ppm detection using Cu-doped SnO$_2$ nanosheet arrays directly grown on chip. *Sens. Actuators B Chem.* **2020**, *324*, 128745. [CrossRef]

35. Zhang, Z.; Chen, H.; Xing, C.; Guo, M.; Xu, F.; Wang, X.; Gruber, H.J.; Zhang, B.; Tang, J. Sodium citrate: A universal reducing agent for reduction/decoration of graphene oxide with au nanoparticles. *Nano Res.* **2011**, *4*, 599–611. [CrossRef]

36. Chung, M.G.; Kim, D.-H.; Seo, D.K.; Kim, T.; Im, H.U.; Lee, H.M.; Yoo, J.-B.; Hong, S.-H.; Kang, T.J.; Kim, Y.H. Flexible hydrogen sensors using graphene with palladium nanoparticle decoration. *Sens. Actuators B Chem.* **2012**, *169*, 387–392. [CrossRef]

37. Chen, M.-L.; Park, C.-Y.; Choi, J.-G.; Oh, W.-C. Synthesis and Characterization of Metal (Pt, Pd and Fe)-graphene Composites. *J. Korean Ceram. Soc.* **2011**, *48*, 147–151. [CrossRef]

38. Sudha, V.; Murugadoss, G.; Thangamuthu, R. Structural and morphological tuning of Cu-based metal oxide nanoparticles by a facile chemical method and highly electrochemical sensing of sulphite. *Sci. Rep.* **2021**, *11*, 3413. [CrossRef] [PubMed]

39. Zhang, Y.; Tang, H.; Ji, X.; Li, C.; Chen, L.; Zhang, D.; Yang, X.; Zhang, H. Synthesis of reduced graphene oxide/Cu nanoparticle composites and their tribological properties. *RSC Adv.* **2013**, *3*, 26086–26093. [CrossRef]

40. Khan, A.; Rashid, A.; Younas, R.; Chong, R. A chemical reduction approach to the synthesis of copper nanoparticles. *Int. Nano Lett.* **2016**, *6*, 21–26. [CrossRef]

41. Dresselhaus, M.S.; Jorio, A.; Hofmann, M.; Dresselhaus, G.; Saito, R. Perspectives on Carbon Nanotubes and Graphene Raman Spectroscopy. *Nano Lett.* **2010**, *10*, 751–758. [CrossRef]

42. Ding, H.; Zhang, S.; Chen, J.-T.; Hu, X.-P.; Du, Z.-F.; Qiu, Y.-X.; Zhao, D.-L. Reduction of graphene oxide at room temperature with vitamin C for RGO–TiO$_2$ photoanodes in dye-sensitized solar cell. *Thin Solid Film.* **2015**, *584*, 29–36. [CrossRef]

43. Ferrari, A.C.; Meyer, J.C.; Scardaci, V.; Casiraghi, C.; Lazzeri, M.; Mauri, F.; Piscanec, S.; Jiang, D.; Novoselov, K.S.; Roth, S.; et al. Raman Spectrum of Graphene and Graphene Layers. *Phys. Rev. Lett.* **2006**, *97*, 187401. [CrossRef] [PubMed]

44. Cançado, L.G.; Jorio, A.; Ferreira, E.H.M.; Stavale, F.; Achete, C.A.; Capaz, R.B.; Moutinho, M.V.d.O.; Lombardo, A.; Kulmala, T.S.; Ferrari, A.C. Quantifying Defects in Graphene via Raman Spectroscopy at Different Excitation Energies. *Nano Lett.* **2011**, *11*, 3190–3196. [CrossRef] [PubMed]

45. Mishra, M.; Singh, A.P.; Singh, B.P.; Dhawan, S.K. Performance of a nanoarchitectured tin oxide@reduced graphene oxide composite as a shield against electromagnetic polluting radiation. *RSC Adv.* **2014**, *4*, 25904–25911. [CrossRef]

46. Kolmakov, A.; Klenov, D.O.; Lilach, Y.; Stemmer, S.; Moskovits, M. Enhanced Gas Sensing by Individual SnO$_2$ Nanowires and Nanobelts Functionalized with Pd Catalyst Particles. *Nano Lett.* **2005**, *5*, 667–673. [CrossRef] [PubMed]

47. Pandey, P.; Sui, M.; Zhang, Q.; Li, M.-Y.; Kunwar, S.; Lee, J. Systematic control of the size, density and configuration of Pt nanostructures on sapphire (0001) by the variation of deposition amount and dwelling time. *Appl. Surf. Sci.* **2016**, *368*, 198–207. [CrossRef]

48. Fowler, J.D.; Allen, M.J.; Tung, V.C.; Yang, Y.; Kaner, R.B.; Weiller, B.H. Practical Chemical Sensors from Chemically Derived Graphene. *ACS Nano* **2009**, *3*, 301–306. [CrossRef]

49. Bøggild, P.; Mackenzie, D.M.; Whelan, P.R.; Petersen, D.H.; Buron, J.D.; Zurutuza, A.; Gallop, J.; Hao, L.; Jepsen, P.U. Mapping the electrical properties of large-area graphene. *2D Materials* **2017**, *4*, 042003. [CrossRef]

50. Huh, S.; Park, J.; Kim, K.S.; Hong, B.H.; Kim, S.B. Selective n-Type Doping of Graphene by Photo-patterned Gold Nanoparticles. *ACS Nano* **2011**, *5*, 3639–3644. [CrossRef]

51. Duan, Y.; Teplyakov, A.V. Deposition of copper from Cu(i) and Cu(ii) precursors onto HOPG surface: Role of surface defects and choice of a precursor. *J. Chem. Phys.* **2017**, *146*, 052814. [CrossRef]

52. Goncalves, G.; Marques, P.A.A.P.; Granadeiro, C.M.; Nogueira, H.I.S.; Singh, M.K.; Grácio, J. Surface Modification of Graphene Nanosheets with Gold Nanoparticles: The Role of Oxygen Moieties at Graphene Surface on Gold Nucleation and Growth. *Chem. Mater.* **2009**, *21*, 4796–4802. [CrossRef]

53. Giovannetti, G.; Khomyakov, P.A.; Brocks, G.; Karpan, V.M.; van den Brink, J.; Kelly, P.J. Doping Graphene with Metal Contacts. *Phys. Rev. Lett.* **2008**, *101*, 026803. [CrossRef] [PubMed]

54. Benayad, A.; Shin, H.-J.; Park, H.K.; Yoon, S.-M.; Kim, K.K.; Jin, M.H.; Jeong, H.-K.; Lee, J.C.; Choi, J.-Y.; Lee, Y.H. Controlling work function of reduced graphite oxide with Au-ion concentration. *Chem. Phys. Lett.* **2009**, *475*, 91–95. [CrossRef]

55. Xiang, J.; Drzal, L.T. Electron and Phonon Transport in Au Nanoparticle Decorated Graphene Nanoplatelet Nanostructured Paper. *ACS Appl. Mater. Interfaces* **2011**, *3*, 1325–1332. [CrossRef]

56. Chatterjee, S.G.; Chatterjee, S.; Ray, A.K.; Chakraborty, A.K. Graphene–metal oxide nanohybrids for toxic gas sensor: A review. *Sens. Actuators B Chem.* **2015**, *221*, 1170–1181. [CrossRef]

57. Chowdhury, N.K.; Bhowmik, B. Micro/nanostructured gas sensors: The physics behind the nanostructure growth, sensing and selectivity mechanisms. *Nanoscale Adv.* **2021**, *3*, 73–93. [CrossRef]

58. Ciftyurek, E.; Li, Z.; Schierbaum, K. Adsorbed Oxygen Ions and Oxygen Vacancies: Their Concentration and Distribution in Metal Oxide Chemical Sensors and Influencing Role in Sensitivity and Sensing Mechanisms. *Sensors* **2023**, *23*, 29. [CrossRef]

59. Drewniak, S.; Drewniak, Ł.; Pustelny, T. Mechanisms of NO$_2$ Detection in Hybrid Structures Containing Reduced Graphene Oxide: A Review. *Sensors* **2022**, *22*, 5316. [CrossRef]

60. Vuong, N.M.; Kim, D.; Kim, H. Porous Au-embedded WO$_3$ Nanowire Structure for Efficient Detection of CH$_4$ and H$_2$S. *Sci. Rep.* **2015**, *5*, 11040. [CrossRef]

61. Haridas, D.; Gupta, V. Enhanced response characteristics of SnO_2 thin film based sensors loaded with Pd clusters for methane detection. *Sens. Actuators B Chem.* **2012**, *166–167*, 156–164. [CrossRef]
62. Shen, F.; Wang, D.; Liu, R.; Pei, X.; Zhang, T.; Jin, J. Edge-tailored graphene oxide nanosheet-based field effect transistors for fast and reversible electronic detection of sulfur dioxide. *Nanoscale* **2013**, *5*, 537–540. [CrossRef] [PubMed]
63. Han, L.; Liu, C.-M.; Dong, S.-L.; Du, C.-X.; Zhang, X.-Y.; Li, L.-H.; Wei, Y. Enhanced conductivity of rGO/Ag NPs composites for electrochemical immunoassay of prostate-specific antigen. *Biosens. Bioelectron.* **2017**, *87*, 466–472. [CrossRef] [PubMed]
64. Zeng, S.; Zhang, Y.; Zhang, Y.; Li, Y.; Tang, C.; Li, K.; Sun, J.; Deng, T. A novel room temperature SO_2 gas sensor based on TiO_2/rGO buried-gate FET. *Microelectron. Eng.* **2022**, *263*, 111841. [CrossRef]
65. Prezioso, S.; Perrozzi, F.; Giancaterini, L.; Cantalini, C.; Treossi, E.; Palermo, V.; Nardone, M.; Santucci, S.; Ottaviano, L. Graphene Oxide as a Practical Solution to High Sensitivity Gas Sensing. *J. Phys. Chem. C* **2013**, *117*, 10683–10690. [CrossRef]
66. Zhang, H.; Cen, W.; Liu, J.; Guo, J.; Yin, H.; Ning, P. Adsorption and oxidation of SO_2 by graphene oxides: A van der Waals density functional theory study. *Appl. Surf. Sci.* **2015**, *324*, 61–67. [CrossRef]